

# AMBER-NACO aperture-synthesis imaging of the half-obscured central star and the edge-on disk of the red giant L<sub>2</sub> Pup<sup>★</sup>

K. Ohnaka<sup>1,2</sup>, D. Schertl<sup>2</sup>, K.-H. Hofmann<sup>2</sup>, and G. Weigelt<sup>2</sup>

<sup>1</sup> Universidad Católica del Norte, Instituto de Astronomía, Avenida Angamos 0610, Antofagasta, Chile  
e-mail: k1.ohnaka@gmail.com

<sup>2</sup> Max-Planck-Institut für Radioastronomie, Auf dem Hügel 69, 53121 Bonn, Germany

Received / Accepted

## ABSTRACT

**Aims.** The red giant L<sub>2</sub> Pup started a dimming event in 1994, which is considered to be caused by the ejection of dust clouds. We present near-IR aperture-synthesis imaging of L<sub>2</sub> Pup achieved by combining data from VLT/NACO and the AMBER instrument of the Very Large Telescope Interferometer (VLTI). Our aim is to spatially resolve the innermost region of the circumstellar environment. **Methods.** We carried out speckle interferometric observations at 2.27  $\mu\text{m}$  with VLT/NACO and long-baseline interferometric observations with VLTI/AMBER at 2.2–2.35  $\mu\text{m}$  with baselines of 15–81 m. We also extracted an 8.7  $\mu\text{m}$  image from the mid-IR VLTI instrument MIDI.

**Results.** The diffraction-limited image obtained by bispectrum speckle interferometry with NACO with a spatial resolution of 57 mas shows an elongated component. The aperture-synthesis imaging combining the NACO speckle data and AMBER data with a spatial resolution of 5.6 $\times$ 7.3 mas further resolves not only this elongated component, but also the central star. The reconstructed image reveals that the elongated component is a nearly edge-on disk with a size of  $\sim 180 \times 50$  mas lying in the E-W direction, and furthermore, that the southern hemisphere of the central star is severely obscured by the equatorial dust lane of the disk. The angular size of the disk is consistent with the distance that the dust clouds that were ejected at the onset of the dimming event should have traveled by the time of our observations, if we assume that the dust clouds moved radially. This implies that the formation of the disk may be responsible for the dimming event. The 8.7  $\mu\text{m}$  image with a spatial resolution of 220 mas extracted from the MIDI data taken in 2004 (seven years before the AMBER and NACO observations) shows an approximately spherical envelope without a signature of the disk. This suggests that the mass loss before the dimming event may have been spherical.

**Key words.** infrared: stars – techniques: interferometric – stars: imaging – stars: AGB and post-AGB – (stars:) circumstellar matter – stars: individual: L<sub>2</sub> Pup

## 1. Introduction

Slow, but intense mass loss at the asymptotic giant branch (AGB) leads to the formation of thick circumstellar envelopes. When AGB stars evolve further to protoplanetary nebulae (PPNe) and planetary nebulae (PNe), striking bipolar lobes emerge, often accompanied by collimated jets (Sahai & Trauger 1998). Binarity is currently considered to be the most promising mechanism to shape PNe (e.g., De Marco 2009), but it is not yet understood how and at which evolutionary phase the bipolar structure emerges. High-resolution imaging of a few dusty AGB stars reveals bipolar or more complex, clumpy structures (e.g., Weigelt et al. 1998; Monnier et al. 2000; Hofmann et al. 2001). Some AGB stars show spiral structures, which strongly suggests the influence of a companion (e.g., Mauron & Huggins 2006; Maercker et al. 2012; Kim et al. 2013; Ramstedt et al. 2014; Mayer et al. 2014; Decin et al. 2015). These observations suggest that the seed of the morphological change already exists in the AGB phase.

The M5 giant L<sub>2</sub> Pup is a bright, nearby AGB star with a mass-loss rate of  $\sim 3 \times 10^{-7} M_{\odot} \text{ yr}^{-1}$  (Jura et al. 2002) that shows episodic, asymmetric dust formation. Magalhães et al. (1986) interpreted temporally variable polarization in the optical as due to the growth and dissipation of dust grains in an asymmetric dust cloud. The 11.7 and 17.9  $\mu\text{m}$  images of Jura et al. (2002) showed an asymmetric circumstellar dust envelope. Furthermore, Bedding et al. (2002) have detected a dimming event in the optical light curve of L<sub>2</sub> Pup starting in 1994, which suggests the ejection of dust clouds. The brightness profiles reconstructed in the visible also lend support to the hypothesis that there are asymmetric dust clouds close to the star (Ireland et al. 2004).

The circumstellar environment of L<sub>2</sub> Pup close to the star has recently been investigated in more detail. Kervella et al. (2014, hereafter K14) observed L<sub>2</sub> Pup using the adaptive optics instrument NACO at VLT. Their images taken from 1.04 to 4.05  $\mu\text{m}$  with a spatial resolution from 26 to 100 mas reveal a nearly edge-on disk lying in the E-W direction. The authors also showed that the observed images can be explained well by a flared disk model. The 2.30 and 3.74  $\mu\text{m}$  images obtained by Lykou et al. (2015, hereafter L15) using the aperture-masking technique with NACO also show an elongated component. More recently, Kervella et al. (2015) have revealed a clear bipolar structure using the VLT/SPHERE-ZIMPOL instrument.

Send offprint requests to: K. Ohnaka

<sup>★</sup> Based on AMBER, NACO, and MIDI observations made with the Very Large Telescope and Very Large Telescope Interferometer of the European Southern Observatory. Program ID: 074.D-0075(A), 074.D-0101(A), 074.D-0198(B), 088.D-0150(A/B), and 288.D-5041(A)

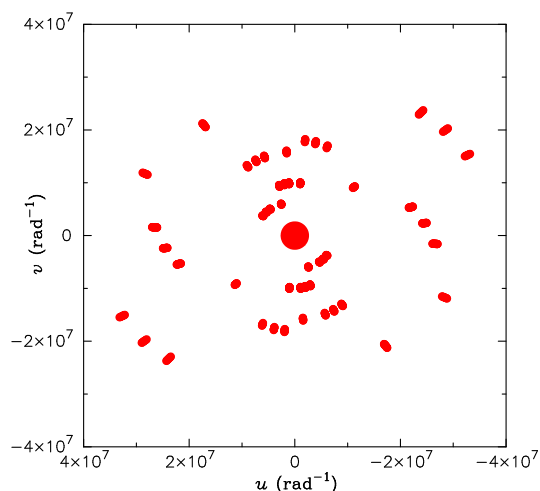


**Fig. 1.**  $uv$  coverage of our AMBER and NACO speckle observations of L<sub>2</sub> Pup.

In this paper, we present near-IR interferometric observations of L<sub>2</sub> Pup with an even higher spatial resolution of  $5.6 \times 7.3$  mas, combining VLT/NACO and the near-IR interferometric instrument AMBER at the Very Large Telescope Interferometer (VLTI). In addition, we also present a mid-IR image at  $8.7 \mu\text{m}$  extracted from the mid-IR VLTI instrument MIDI.

## 2. Observations

The near-IR interferometric instrument VLTI/AMBER combines three telescopes and allows us to observe objects with a spatial resolution of  $\sim 3$  mas (at  $2 \mu\text{m}$ ) with the currently available baselines and a spectral resolution of 35, 1500, and 12000 (Petrov et al. 2007). Our AMBER observations of L<sub>2</sub> Pup reported in this paper took place on 2011 December 23, 29, and 30 (UTC) using two different telescope configurations (A1-C1-D0 and D0-H0-I1), which provided projected baseline lengths from 15 to 81 m (Program ID: 088.D-0150A/B). The  $uv$  coverage is shown in Fig. 1. We used the medium spectral resolution of 1500 in the wavelength region between 2.2 and  $2.35 \mu\text{m}$ , covering the continuum and the CO first overtone bands. The Detector Integration Time (DIT) was set to 100 ms in all AMBER data sets. We observed Sirius ( $\alpha$  CMa, A1V, uniform-disk diameter = 5.9 mas; Davis et al. 2011) and Rigel ( $\beta$  Ori, B8Iae, uniform-disk diameter = 2.43 mas; Richichi et al. 2005) as interferometric calibrators.

Additionally, we carried out speckle interferometric observations with VLT/NACO in Director’s Discretionary Time to obtain interferometric data at short baselines (Program ID: 288.D-5041A). This is crucial for the aperture-synthesis imaging of objects with a very extended component. The NACO speckle observations reported here occurred on 2012 March 21 with the IB2.27 filter, which is centered at  $2.27 \mu\text{m}$  with a FWHM of  $0.06 \mu\text{m}$ . We recorded 398 frames with DIT = 109 ms using the S13 camera with a pixel scale of 13.2 mas. The window size was  $512 \times 514$  pixels, which resulted in a field of view of  $6''.8 \times 6''.8$ . We observed Canopus ( $\alpha$  Car, A9II, angular diameter = 6.9 mas; Domiciano de Souza et al. 2008) as a calibrator and took 300 frames with the same DIT as L<sub>2</sub> Pup.

As complementary data, we also extracted mid-IR images at  $8.7 \mu\text{m}$  (filter FWHM =  $1.75 \mu\text{m}$ ) from the acquisition image data obtained with the VLTI/MIDI instrument (Leinert et al.

2003). These images were taken to adjust the position of the target on the detector. Thanks to the adaptive optics system for the MIDI operation with the 8.2 m Unit Telescopes (UTs) and the short DIT of 4 ms, the MIDI acquisition images are diffraction limited. In the ESO archive, there are MIDI data of L<sub>2</sub> Pup taken on 2004 December 31, 2005 January 3, 2005 February 28, and 2005 March 3 (the interferometric data obtained on 2005 January 3 (UTC) are presented in K14). The data taken on 2004 December 31 with UT3 and UT4 (Program ID: 074.D-0198B) provide the best images of L<sub>2</sub> Pup and the calibrators, which are used as references of the point spread function (PSF), and we therefore present only these images in this paper. We reduced the data of  $\epsilon$  Cru and S Ori obtained on the same night to ascertain the PSF (Program IDs: 074.D-0101A and 074.D-0075A). As we show below (Fig. 4), the quality of the PSF obtained from the data of  $\epsilon$  Cru is noticeably poorer than the image quality of L<sub>2</sub> Pup because the former star is much fainter ( $F_{12 \mu\text{m}} = 32.4$  Jy) than the latter ( $F_{12 \mu\text{m}} = 2415$  Jy). As a second PSF, we therefore used the Mira star S Ori because its mid-IR flux ( $F_{12 \mu\text{m}} = 151$  Jy) is much higher than  $\epsilon$  Cru. Although S Ori was observed as a science target of interferometric observations, it is unresolved in the acquisition images at  $8.7 \mu\text{m}$ , as we show below. The summary of our AMBER and NACO observations as well as the MIDI observations is given in Table. 1.

We reduced the AMBER data with the amdlib ver. 3.0.3 package<sup>1</sup>, which is based on the P2VM algorithm (Tatulli et al. 2007). The product of the reduction is the visibility (or visibility amplitude), closure phase, and differential phase. We binned the raw data in the spectral direction with a box car filter with a width of three pixels to increase the S/N ratio. The details of the reduction are described in Ohnaka et al. (2009). We excluded the data sets #2, #6–9, #13, and #15. They were taken under poor and variable seeing ( $\geq 1''.5$ ) and/or short coherence time ( $\leq 3.0$  ms), which makes the absolute calibration of the visibilities unreliable. The NACO data were reduced with the bispectrum speckle interferometry method (Weigelt 1977; Lohmann et al. 1983; Hofmann & Weigelt 1986). The result of the reduction of speckle data is the 2D visibility, the bispectrum on a huge number of baseline triangles within the maximum baseline of 8 m (aperture of the telescope), and a reconstructed image of the object. For the combined image reconstruction with AMBER and NACO, we sampled visibilities and closure phases from the speckle data on randomly selected 855 baseline triangles within a maximum baseline length of 6 m (we avoided sampling between 6 and 8 m because the data are noisy).

For the reconstruction of an aperture-synthesis image from the combined AMBER and NACO speckle data, we used the image reconstruction package MiRA<sup>2</sup> (Thiébaud 2008), which was also used for the image reconstruction of the red supergiants Betelgeuse and Antares in our previous works (Ohnaka et al. 2011, 2013). Given that the wavelengths covered by AMBER and NACO overlap ( $2.2$ – $2.35$  and  $2.27 \mu\text{m}$ , respectively), it can be justified to combine the AMBER and NACO data for the image reconstruction in the continuum. We used all wavelengths in the continuum region ( $2.2$ – $2.29 \mu\text{m}$ ) in the AMBER data to reconstruct one image because the object image is not expected to change noticeably in this narrow continuum region. Details of the image reconstruction procedure we adopted are described in Appendix B.

The reduction of the MIDI acquisition images is similar to the processing described in Ohnaka (2014). After the sky sub-

<sup>1</sup> [http://www.jmmc.fr/data\\_processing\\_amber.htm](http://www.jmmc.fr/data_processing_amber.htm)

<sup>2</sup> <http://cral.univ-lyon1.fr/labo/perso/eric.thiebaut/?Software/MiRA>

**Table 1.** Summary of the AMBER and NACO speckle observations and the archived MIDI data of L<sub>2</sub> Pup. The seeing, which was measured with a differential image motion monitor (DIMM), and the coherence time ( $\tau_0$ ) were measured in the visible (see for details <http://www.eso.org/gen-fac/pubs/astclim/paranal/seeing/adaptive-optics/>).  $N_f$  is the number of frames, and  $N_{\text{exp}}$  is the number of exposures.

#	$t_{\text{obs}}$ (UTC)	$B_p$ (m)	PA ( $^\circ$ )	Seeing ( $''$ )	$\tau_0$ (ms)	DIT $\times$ $N_f \times N_{\text{exp}}$ (ms)	Remarks
AMBER (A1-C1-D0): L <sub>2</sub> Pup: 2011 Dec 23 (UTC)							
1	01:48:07	35.7/14.5/22.3	-175/23/174	0.9	4.0	100 $\times$ 500 $\times$ 5	
2	02:33:57	35.7/14.9/22.3	-166/34/-180	1.7	2.5	100 $\times$ 500 $\times$ 5	Not used
3	03:11:28	35.8/15.3/22.3	-160/42/-174	1.2	3.0	100 $\times$ 500 $\times$ 5	
4	03:47:56	35.8/15.6/22.2	-153/50/-169	0.9	3.7	100 $\times$ 500 $\times$ 5	
5	04:24:20	35.7/15.9/22.1	-147/57/-164	1.1	3.5	100 $\times$ 500 $\times$ 10	
6	06:00:50	34.4/15.8/21.4	-132/74/-151	1.7	1.7	100 $\times$ 500 $\times$ 10	Not used
7	07:04:38	32.5/15.1/20.5	-123/85/-144	2.2	1.3	100 $\times$ 500 $\times$ 15	Not used
8	07:23:33	31.8/14.7/20.2	-121/88/-142	2.2	1.4	100 $\times$ 500 $\times$ 10	Not used
9	08:41:54	27.4/12.8/18.2	-111/103/-134	2.7	1.1	100 $\times$ 500 $\times$ 5	Not used
C1	01:19:52	30.2/10.3/21.5	-174/33/173	0.8	4.7	100 $\times$ 1000 $\times$ 5	Sirius
C2	02:16:06	31.0/12.0/21.5	-162/47.5/-178	0.9	4.1	100 $\times$ 500 $\times$ 5	Sirius
C3	03:30:29	33.1/14.3/21.7	-149/60/-167	0.9	4.1	100 $\times$ 500 $\times$ 5	Sirius
C4	04:06:45	34.2/15.1/22.0	-144/64/-162	0.8	4.7	100 $\times$ 500 $\times$ 5	Sirius
C5	04:50:11	35.2/15.8/22.3	-138/69/-157	1.3	2.7	100 $\times$ 500 $\times$ 10	Sirius
AMBER (D0-H0-I1): 2011 Dec 29 (UTC)							
10	06:46:01	81.0/40.0/60.0	114/-21/86	0.9	7.0	100 $\times$ 500 $\times$ 8	
11	07:38:25	78.1/40.4/55.6	124/-13/95	0.9	6.0	100 $\times$ 500 $\times$ 5	
12	08:20:26	75.1/40.5/51.0	134/-67/103	0.9	6.5	100 $\times$ 500 $\times$ 5	
13	08:56:34	72.3/40.5/46.6	142/-104/111	1.0-1.7	4.4	100 $\times$ 500 $\times$ 5	Not used
C6	06:23:18	76.7/39.2/61.1	107/-205/77	1.0	5.8	100 $\times$ 500 $\times$ 5	Sirius
C7	07:10:38	69.8/38.5/56.3	113/-137/79	2.0	2.8	100 $\times$ 500 $\times$ 1	Sirius
C8	07:20:40	73.1/40.6/49.0	136/-44/105	1.2	4.6	100 $\times$ 500 $\times$ 5	Sirius
AMBER (D0-H0-I1): 2011 Dec 30 (UTC)							
14	02:28:00	68.4/32.2/60.5	67/-51/39	0.7	6.0	100 $\times$ 500 $\times$ 5	
15	05:23:07	82.2/39.0/63.6	100/-32/72	1.5	2.7	100 $\times$ 500 $\times$ 5	Not used
C9	00:09:57	58.5/39.5/42.5	95/-39/52	1.2	3.8	100 $\times$ 500 $\times$ 5	Rigel
C10	01:10:28	50.7/36.8/43.2	83/-40/38	1.1	4.1	100 $\times$ 500 $\times$ 5	Sirius
C11	01:52:41	61.3/38.5/48.6	87/-40/48	0.9	4.7	100 $\times$ 500 $\times$ 5	Sirius
C12	03:47:19	81.4/39.0/64.0	101/-29/73	0.6	7.6	100 $\times$ 500 $\times$ 5	Rigel
NACO: 2012 Mar 21 (UTC)							
16	02:30:14	—	—	1.6	3.0	109 $\times$ 398 $\times$ 1	
C13	02:38:11	—	—	2.0	3.0	109 $\times$ 300 $\times$ 1	Canopus
MIDI (UT3-UT4): 2004 Dec 31 (UTC)							
17	03:19:33	—	—	1.2	2.3	4 $\times$ 1000 $\times$ 2	Acquisition images
18	05:02:14	—	—	1.7	1.5	4 $\times$ 1000 $\times$ 2	Acquisition images
C14	01:47:07	—	—	1.1	2.6	4 $\times$ 1000 $\times$ 2	S Ori
C15	02:37:28	—	—	0.8	3.6	4 $\times$ 1000 $\times$ 1	S Ori
C16	07:09:13	—	—	0.9	2.7	4 $\times$ 1000 $\times$ 2	$\epsilon$ Cru

traction, we recentered each frame and added the frames. The sky-subtracted images of L<sub>2</sub> Pup show detector artifacts that are presumably caused by the high brightness of L<sub>2</sub> Pup. After removing these artifacts as described in Appendix A, we added all frames in each data set of L<sub>2</sub> Pup. The calibrators are much fainter than L<sub>2</sub> Pup, and the residual of the sky subtraction is significant in some frames. Therefore, we only added the frames in which the residual of the sky subtraction is small, to obtain as clean a PSF as possible. The resulting image from each data set was derotated so that North is up and East is to the left, using the field rotation angle (Mathar 2006). Finally, the derotated images from all data sets were added. The quality of the images taken with UT3 is significantly lower than that taken with UT4, therefore we present the final image obtained from the UT4 data. We carried out neither the PSF subtraction nor the deconvolution because the images of L<sub>2</sub> Pup are saturated at the central peak.

### 3. Results

#### 3.1. Near-IR AMBER-NACO aperture-synthesis image

Figure 2 shows the images reconstructed from the NACO speckle data alone and from the combined NACO speckle and AMBER data. Both images are convolved with the following Gaussian beam. The beam size (FWHM) of the image reconstructed from the speckle data alone is 57 mas, which corresponds to the diffraction-limit of VLT at 2.27  $\mu\text{m}$ . The beam size of the image reconstructed from the combined data is 5.6  $\times$  7.3 mas, which was derived by fitting the central peak of the dirty beam with a 2D elliptical Gaussian. Figure 3 shows a comparison of the visibilities and closure phases from the reconstructed image with the observed data. The reduced  $\chi^2$  of the fit is 0.97. The image reconstructed from the speckle data alone shows a central star and an extended component elongated approximately in the E-W direction with a size of  $\sim 300 \times 200$  mas.

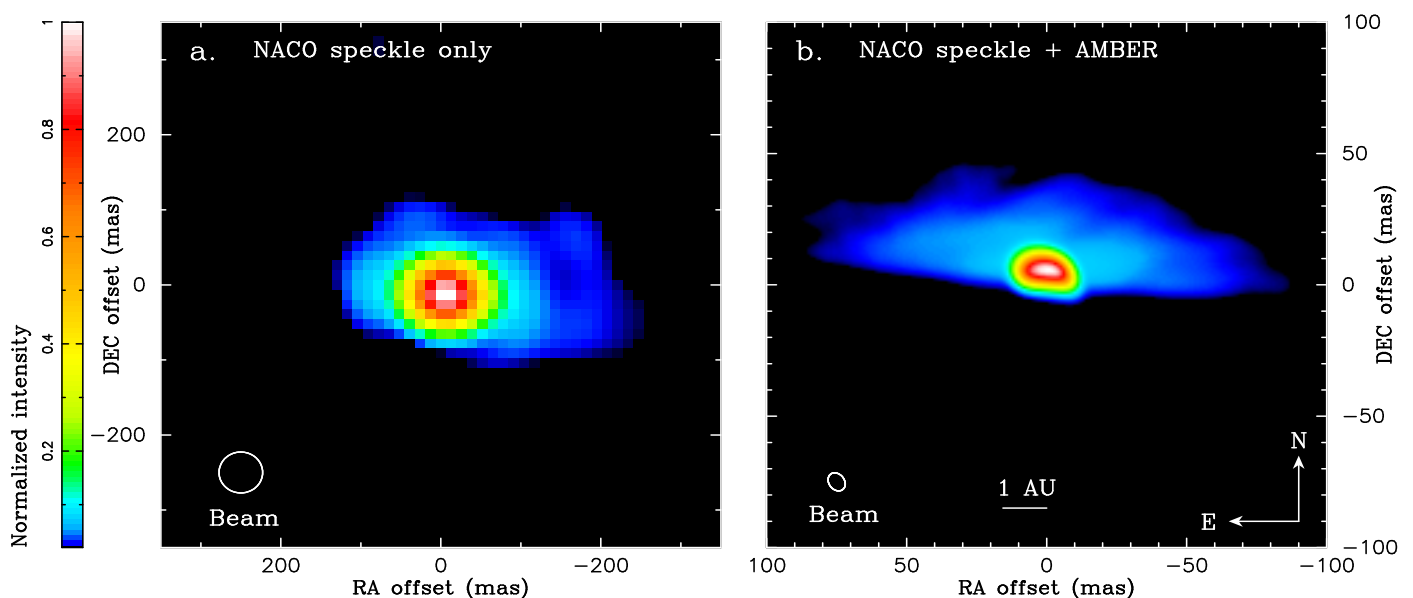


**Fig. 2.** **a:** Image of L<sub>2</sub> Pup reconstructed from the NACO speckle data alone. **b:** Image reconstructed from the combined AMBER and NACO speckle data.

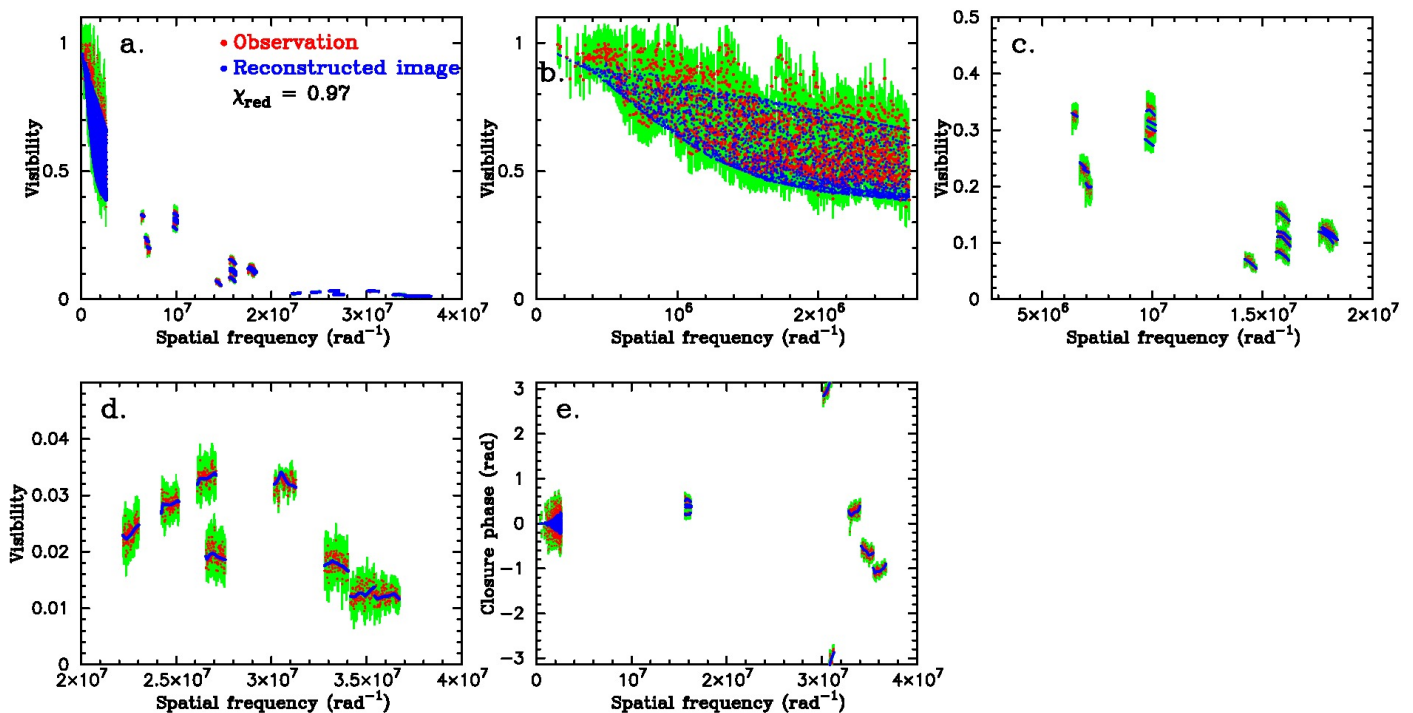


**Fig. 3.** Comparison of the observed interferometric data and the corresponding observables from the reconstructed image shown in Fig. 2b (a color version of the figure is available in the electronic edition). The observed data are plotted with the red (black in the printed edition) symbols with the error bars shown in green (light gray), while the model is represented by the blue (dark gray) symbols. **a:** Visibilities. **b:** Enlarged view of the visibilities obtained by speckle interferometry with NACO. **c** and **d:** Enlarged views of the visibilities obtained with AMBER in two different spatial frequency ranges. **e:** Closure phases.

The size of the extended component in the deconvolved images obtained by K14 and L15 in the *K* band is  $\sim 200 \times 100$  mas, which roughly agrees with the measured size in our speckle image, which is convolved with the aforementioned beam.

The image reconstructed from the combined NACO speckle and AMBER data, shown in Fig. 2b, further resolves not only the elongated component seen in the speckle image, but also the central star. In this image, the extended component has a size of  $\sim 180 \times 50$  mas. We checked that the NACO speckle + AMBER

image matches the NACO speckle-only image when convolved with the corresponding beam. Moreover, the figure shows that the southern half of the central star is severely obscured. This AMBER–NACO aperture-synthesis image directly shows both the edge-on disk and the half-observed central star due to the equatorial dust lane of the disk. At the distance of  $64 \pm 4$  pc (from the Hipparcos parallax of  $15.61 \pm 0.99$  mas, van Leeuwen 2007), the imaged size of the disk corresponds to  $(11.5 \pm 0.8) \times (2.8 \pm 0.2)$  AU.

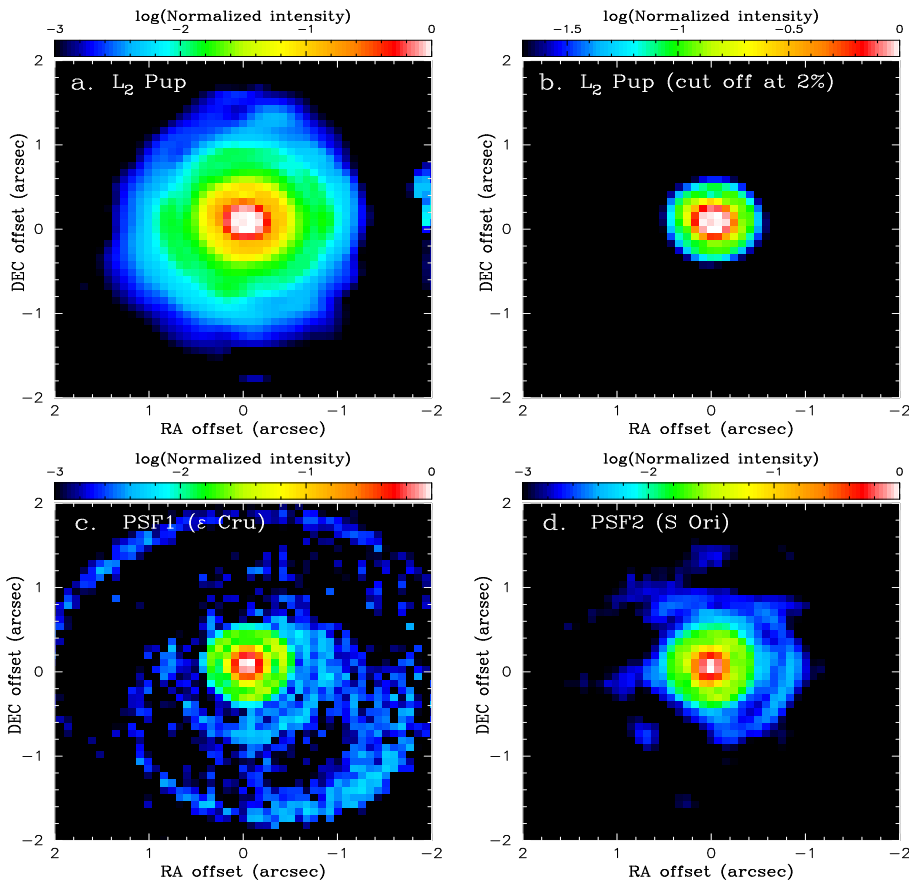


**Fig. 4.** 8.7  $\mu\text{m}$  images of L<sub>2</sub> Pup and two PSF reference stars extracted from the MIDI acquisition data. In all panels, North is up and East is to the left. **a:** L<sub>2</sub> Pup with a minimum intensity of 0.1% of the central peak. **b:** L<sub>2</sub> Pup with a minimum intensity of 2% of the central peak to compare with the 11.7  $\mu\text{m}$  image obtained by Jura et al. (2002). **c:** PSF reference star  $\varepsilon$  Cru. The large arcs near the top and the bottom of the image are the residual of the background subtraction. **d:** PSF reference star S Ori.

Our combined aperture-synthesis image is qualitatively consistent with the disk model of K14. They also found out that the 2–2.4  $\mu\text{m}$  interferometric data of L<sub>2</sub> Pup taken in 2001 by the VLTI/VINCI instrument are better fitted with an ellipse with an axis ratio of 1.5 with the major axis at a position angle 106° (i.e., nearly in the E-W direction). This is naturally explained by the obscuration of the southern half of the central star by the edge-on disk, which makes the star appear to be elongated in the E-W direction.

Our AMBER data cover the wavelength region of the CO first overtone bands. However, the speckle data were taken only in the continuum at 2.27  $\mu\text{m}$ , not in the CO bands. This makes the image reconstruction more difficult, if not impossible, in the CO bands. Therefore, the analysis of the AMBER data in the CO bands will be presented in a separate, forthcoming paper.

We note that the obscuration of the central star by a dust disk was also imaged for the eclipsing binary  $\varepsilon$  Aur in the *H* band (1.50–1.74  $\mu\text{m}$ ) by Kloppenborg et al. (2010). In contrast to L<sub>2</sub> Pup, however, the disk of  $\varepsilon$  Aur is located around an orbiting companion, and the disk itself is not visible at least in the *H* band.

### 3.2. Mid-IR MIDI acquisition image

Figure 4 shows the 8.7  $\mu\text{m}$  images of L<sub>2</sub> Pup and the PSF reference stars extracted from the MIDI acquisition data. The image of the first PSF reference  $\varepsilon$  Cru (Fig. 4c) shows noticeable residual of the background subtraction, particularly near the edge of the field of view (large arcs near the top and bottom of the image). The image of the second PSF reference star S Ori is much better, and as Fig. 5 shows, the azimuthally averaged intensity profiles of two PSF reference stars agree, given the poorer qual-

ity of the  $\varepsilon$  Cru image. The FWHM of the intensity profiles of the PSF references indicates a spatial resolution of 220 mas, which corresponds to the diffraction limit at 8.7  $\mu\text{m}$ . The image of L<sub>2</sub> Pup (Fig. 4a) as well as the azimuthally averaged intensity profile (Fig. 5) clearly shows an envelope much more extended than the PSF references. The envelope extends to an angular radius of  $\sim 1''.5$  at the 0.1% intensity of the (saturated) central peak. Figure 4b shows the image of L<sub>2</sub> Pup with an intensity cutoff of 2% of the central peak, in the same manner as the 11.7  $\mu\text{m}$  image presented by Jura et al. (2002, see their Fig. 2). Their 11.7  $\mu\text{m}$  image taken February 2001 (i.e., about four years before the MIDI data) shows an envelope with a radius of  $\sim 1''$ , while our MIDI acquisition image at 8.7  $\mu\text{m}$  is much more compact with a radius of  $\sim 0''.5$  when shown with the same intensity cutoff<sup>3</sup>. This is probably because we probe the inner region of the envelope at 8.7  $\mu\text{m}$  than at 11.7  $\mu\text{m}$ . For this reason, we cannot draw a conclusion about time variations in the envelope between February 2001 and December 2004. In marked contrast to the near-IR image presented above, the mid-IR image appears approximately spherical without a signature of the disk. We discuss this point in Sect. 4.3.

## 4. Discussion

### 4.1. Comparison with the radiative transfer model of K14

To examine whether our aperture-synthesis image of L<sub>2</sub> Pup is quantitatively consistent with the 2D radiative transfer (RT) disk model of K14, we compared the measured interferometric

<sup>3</sup> The central peak of the L<sub>2</sub> Pup image is saturated. If it were not for the saturation, the image with the 2% intensity cutoff would appear even more compact than shown in Fig. 4b.

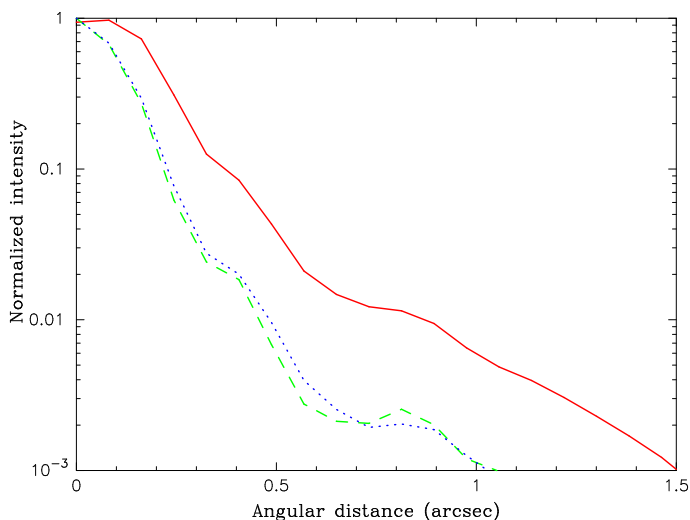


**Fig. 5.** Azimuthally averaged intensity profile of L<sub>2</sub> Pup (red solid line) and the PSF references  $\epsilon$  Cru (green dashed line) and S Ori (blue dotted line). The central region of L<sub>2</sub> Pup within 0'1 is saturated.

observables—visibilities and closure phases—and the observed image with those predicted by their disk model. P. Kervella and M. Montargès kindly provided the best-fit model of their paper. From their model at  $2.17 \mu\text{m}$ , which is the closest wavelength to our observations, we computed the visibilities and closure phases at the  $uv$  points of our NACO speckle and AMBER data.

Figure 6 shows a comparison between the observed data and the RT model of K14. While the model reproduces the overall trend of the observed visibilities as a function of spatial frequency, the fit to the data is poor with the reduced  $\chi^2 = 78.6$ . The model image at  $2.17 \mu\text{m}$  convolved with the beam of our NACO+AMBER aperture-synthesis imaging (Fig. 6f) shows that the disk appears fainter and more inclined (i.e., closer to edge-on) compared to the observed image shown in Fig. 2b (the color scale is the same for the model and observed images). The intensity of the disk in our aperture-synthesis image is  $\sim 7\%$  of the central star, while it is  $\sim 2\%$  in the convolved image of the RT model. This means that the flux contribution of the star is higher in the RT model than in the observed image, which also explains that the model visibilities are higher than the observed data at spatial frequencies of  $(7 - 20) \times 10^6 \text{ rad}^{-1}$ .

It is possible that the flux contribution of the central star was higher at the time of the observations of K14 than for our observations. To examine this possibility, we changed the intensity of the star in the RT model image of K14. As Fig. 7 shows, the reduction of the stellar intensity by a factor of 0.6 can improve the match to the reduced  $\chi^2 = 19.2$ . This result suggests that a time variation in the stellar flux by 0.55 magnitude at  $2.2 \mu\text{m}$  between our AMBER and NACO observations (December 2011 and March 2012) and the NACO observations of K14 (March 2013) can at least partially explain the disagreement between the RT model of K14 and our data. The amplitude of the  $K$ -band light curve of L<sub>2</sub> Pup is  $\sim 0.5$  magnitude (Whitelock et al. 2000). Therefore, the variation in the stellar flux may be due to the pulsation of the central star. However, there is still disagreement in the visibilities observed at the longest baselines (Fig. 7d), and the disk appears too inclined compared to the reconstructed image. This implies time variations in the structure of the disk, for example, inclination angle and/or the flaring angle of the disk.

## 4.2. Binary companion

Kervella et al. (2015) have recently found a companion at 32.9 mas (2.1 AU) in west of the central star by adaptive optics polarimetric imaging in the visible with the VLT/SPHERE-ZIMPOL instrument. However, we do not see a signature of the companion in our NACO+AMBER image. A possible reason might be that the companion is too faint at  $2.2 \mu\text{m}$  and/or our  $uv$  coverage is too sparse in the E-W direction, and therefore, we might have failed to detect the signature of the companion in the visibility or closure phase. Alternatively, the companion might have been at a different position at the time of our observations. Kervella et al. (2015) estimated the orbital period to be 1.4–4.6 years. It is possible that the companion was behind the near side of the inner rim of the disk and was invisible at the time of our AMBER and NACO observations.

To set more quantitative constraints on the position and flux of the companion, we added a companion to the reconstructed image and examined the increase in the reduced  $\chi^2$ . The companion was placed at random positions within 100 mas from the central star (corresponding to the AMBER field of view) and with a random flux contribution with respect to the star. We found out that the fit to the observed data is significantly poorer (reduced  $\chi^2 > 2$ ) for a companion with a flux contribution higher than 2.4% of the central star. This sets an upper limit on the flux of the companion at  $2.2 \mu\text{m}$ . On the other hand, we can set no constraints on the position of the companion.

The separation of the companion of 32.9 mas measured by Kervella et al. (2015) corresponds to 3.8 stellar radii, given the angular diameter of 17.5 mas derived by K14. This implies that the primary red giant star may be filling the Roche lobe and may possibly show deformation, as seen in the Roche-lobe-filling systems  $\beta$  Lyr and Algol =  $\beta$  Per (Zhao et al. 2008; Baron et al. 2012). We examined this possibility by introducing elliptical deformation to the central star in the initial model of the image reconstruction. If the major-axis of the star (E-W direction) is longer than the minor-axis (N-S direction) by more than 40%, the reconstructed image cannot reproduce the observed data very well. The observed axis ratio of the Roche-lobe-filling star is  $\sim 1.2$  in the case of  $\beta$  Lyr and Algol (Zhao et al. 2008; Baron et al. 2012). Therefore, our  $uv$  coverage is not sufficiently dense at long baselines to draw a definitive conclusion about the deformation. Aperture-synthesis imaging with a better  $uv$  coverage is necessary to probe the shape of the primary star.

## 4.3. Dimming event and the disk formation

As mentioned in Sect. 1, L<sub>2</sub> Pup started a dimming event around 1994. If the dust clouds formed in 1994 move away at a radial velocity of  $\sim 3 \text{ km s}^{-1}$  (Winters et al. 2002), they should have traveled a distance of  $\sim 11 \text{ AU} \approx 170 \text{ mas}$  by the time of our observations. This is larger than the angular radius of the disk seen at  $2.2 \mu\text{m}$ , but comparable to the radius of the disk seen at  $3\text{--}4 \mu\text{m}$  (K14; L15). This suggests that the disk may have been formed by the dust clouds that have been ejected since the onset of the dimming event. The dust clouds ejected at the very beginning are perhaps already too far away from the star and, therefore, too cold to be detected at  $2.2 \mu\text{m}$ . We note, however, that this argument is based on the assumption that the dust clouds move away radially. The  $3.74 \mu\text{m}$  images obtained by K14 and L15, the  $4.05 \mu\text{m}$  image of K14, and the visible image of Kervella et al. (2015) show a spiral structure, which is presumably caused by the companion. If the dust clouds move along the spiral structure, the radial distance traveled by the dust clouds is smaller

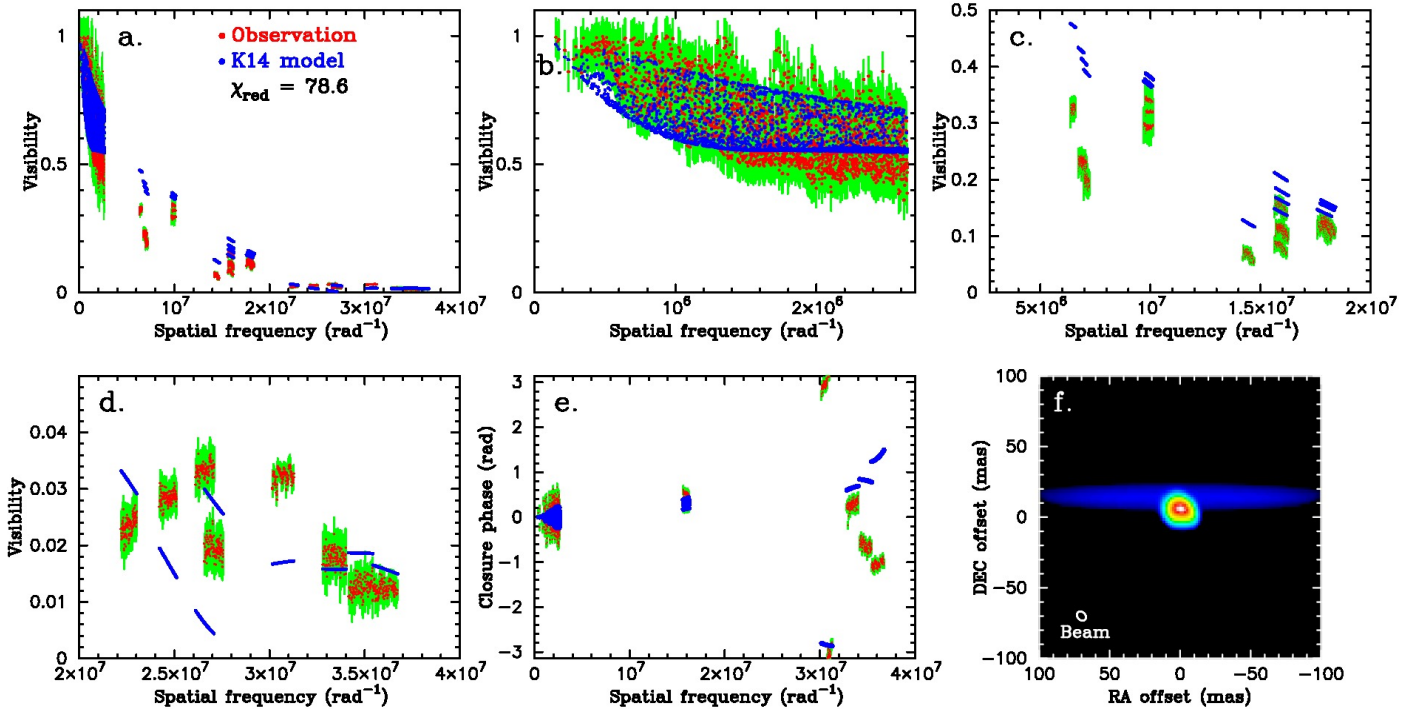


**Fig. 6.** Comparison of our NACO speckle and AMBER observations with the RT model of K14 (a color version of the figure is available in the electronic edition). In panels **a–e**, the observed data are plotted with the red (black in the printed edition) symbols with the error bars shown in green (light gray), while the model is represented by the blue (dark gray) symbols. **a:** Visibilities. **b:** Enlarged view of the visibilities obtained by speckle interferometry with NACO. **c** and **d:** Enlarged views of the visibilities obtained with AMBER in two different spatial frequency ranges. **e:** Closure phases. **f:** Model image in the same color scale as the reconstructed images in Fig. 2.

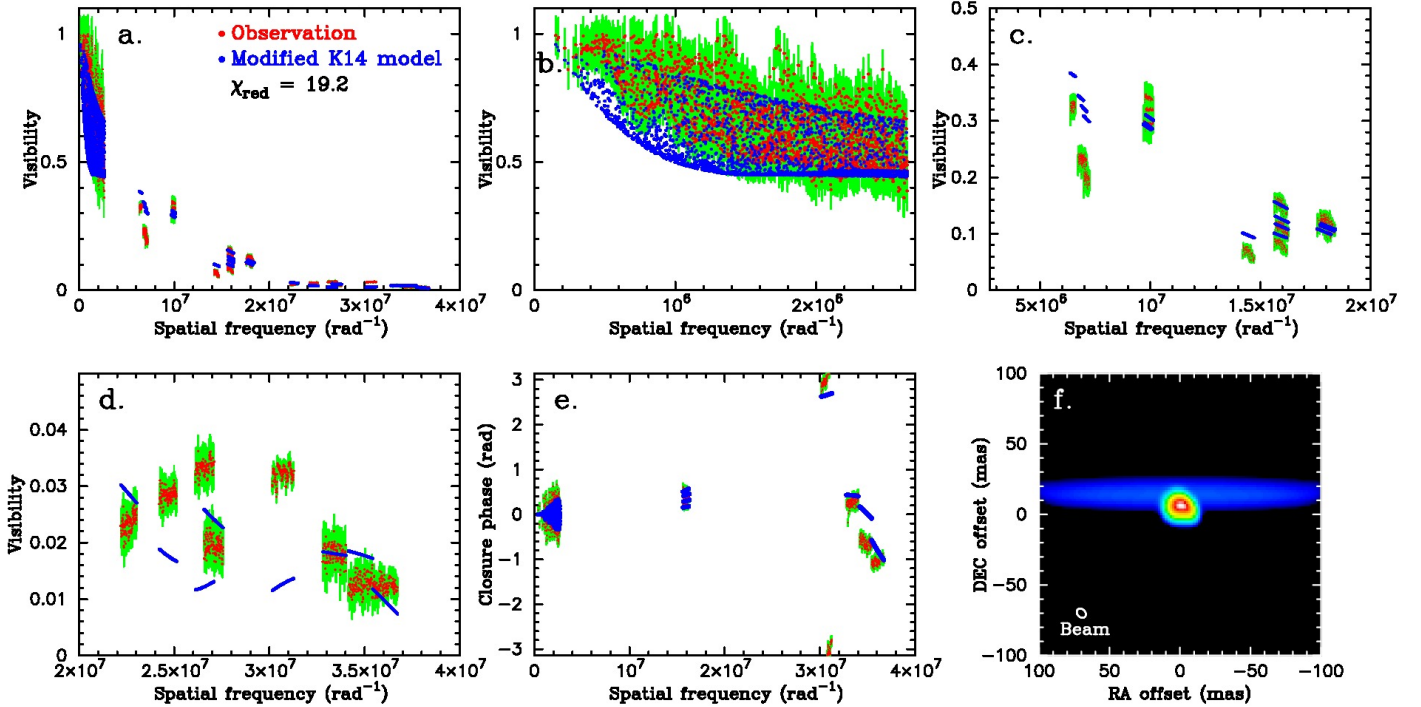


**Fig. 7.** Comparison of our NACO speckle and AMBER observations with the modified RT model of K14, shown in the same manner as in Fig. 6. A color version of the figure is available in the electronic edition.

than estimated above. Therefore, kinematical information of the spiral structure is necessary to confirm the connection between the formation of the disk and the onset of the dimming event.

While the disk seen in the near-IR is oriented roughly in the E-W direction, our mid-IR image at 8.7  $\mu\text{m}$  shown in Fig. 4 as

well as the 11.7  $\mu\text{m}$  and 17.9  $\mu\text{m}$  images presented in Jura et al. (2002) do not show a clear signature of the disk in this direction. Our MIDI acquisition image appears approximately symmetric. The mid-IR images of Jura et al. (2002) are characterized by an elongation at a position angle of  $\sim 135^\circ$  and a distinct blob

at  $225^\circ$ . This makes the object appear slightly elongated in the E-W direction with a size of  $\sim 2''.5 \times 2''.0$ , but the elongation is much less pronounced than seen in the near-IR. Their spatial resolution is  $0''.47$  and  $0''.49$  at  $11.7$  and  $17.9 \mu\text{m}$ , respectively, which is significantly smaller than the angular size of the object, and therefore, the lower spatial resolution cannot fully account for the difference in the morphology. This means that the disk only exists in the innermost region of the circumstellar environment, while the outer region is approximately spherical at least at the time of the observations of Jura et al. (2002) and the MIDI observations.

The mid-IR imaging observations of Jura et al. (2002) took place in February 2001, while the MIDI data were obtained on December 2004. The dust clouds ejected at the onset of the dimming event (around 1994) should have traveled an angular distance of  $\sim 70$  mas (disk diameter of  $\sim 140$  mas) and  $\sim 100$  mas (disk diameter of  $\sim 200$  mas) at the time of Jura et al.'s observations and the MIDI observations, respectively. These angular displacements are smaller or just comparable to the angular resolution of these mid-IR observations, and therefore may have been too small to detect. Furthermore, while we assumed that the dust clouds move away radially, they may actually move along the spiral structure, in which case the radial distance would be smaller. This might also have been a reason for the non-detection of the disk in the mid-IR observations. The circumstellar envelope imaged by these mid-IR observations most likely represents a nearly spherical mass loss that was already present before the formation of the disk.

If we assume that the dust clouds move away radially, the dust clouds ejected at the beginning of the dimming event should have reached an angular distance of  $\sim 200$  mas by now (i.e., the disk diameter of  $\sim 400$  mas), which is resolvable with mid-IR instruments of the current 8–10 m telescopes. If the dust clouds move along the spiral structure, the angular size of the envelope should be smaller. Therefore, new mid-IR imaging would be interesting to examine whether or not the morphology of the circumstellar envelope on larger spatial scales has changed due to the formation of the disk and whether the measured size is consistent with the radial motion of the dust clouds or not.

## 5. Concluding remarks

We have obtained the aperture-synthesis image of both the disk and the central star of L<sub>2</sub> Pup by combining the VLT/NACO speckle data and VLTI/AMBER long-baseline interferometric data. The obtained image shows that the disk has a size of  $\sim 180 \times 50$  mas and the southern half of the central star is severely obscured by the equatorial dust lane of the nearly edge-on disk. This agrees with the recent AO and aperture-masking images and modeling. The observed size of the disk is consistent with the angular distance that the dust clouds formed at the beginning of the dimming event ( $\sim 1994$ ) should have traveled by the time of our observations, if we assume that the dust clouds move away radially. This lends support to the hypothesis that the formation of the dust disk is responsible for the dimming event. However, the kinematical information of the spiral structure is important for establishing the connection between the formation of the disk and the dimming event. ALMA observations of molecular lines are ideal for this goal.

The mid-IR image extracted from the MIDI data taken about seven years before our AMBER and NACO observations shows an approximately spherical envelope, which most likely results from the mass loss occurring before the disk formation. High-resolution mid-IR imaging is useful for studying possible mor-

phological changes in the circumstellar environment on larger spatial scales since the onset of the dimming event.

*Acknowledgements.* We thank the ESO Paranal team for supporting our AMBER and NACO observations. We are also grateful to the ESO's Director General Tim de Zeeuw for allocating our NACO observations in the Director's Discretionary Time and to Pierre Kervella and Miguel Montargès for providing us with their radiative transfer model images.

## References

- Baron, F., Monnier, J. D., Pedretti, E., et al. 2012, *ApJ*, 752, 20  
 Bedding, T. R., Zijlstra, A. A., Jones, A., et al. 2002, *MNRAS*, 337, 79  
 Davis, J., Ireland, M. J., North, J. R., et al. 2011, *PASA*, 28, 58  
 Decin, L., Richards, A. M. S., Neufeld, D., et al. 2015, *A&A*, 574, A5  
 De Marco, O. 2009, *PASP*, 121, 316  
 Domiciano de Souza, A., Bendjoya, P., Vakili, F., Millour, F., & Petrov, R. G. 2008, *A&A*, 489, L5  
 Hofmann, K. H., & Weigelt, G. 1986, *A&A*, 167, L15  
 Hofmann, K. H., & Weigelt, G. 1993, *A&A*, 278, 328  
 Hofmann, K.-H., Balega, Y., Blöcker, T., & Weigelt, G. 2001, *A&A*, 379, 529  
 Ireland, M. J., Tuthill, P. G., Bedding, T. R., Robertson, J. G., & Jacob, A. P. 2004, *MNRAS*, 350, 365  
 Jura, M., Chen, C., & Plavchan, P. 2002, *ApJ*, 569, 964  
 Kervella, P., Montargès, M., Ridgway, S. T., et al. 2014, *A&A*, 564, A88 (K14)  
 Kervella, P., Montargès, M., Lagadec, E., et al. 2015, *A&A*, 578, A77  
 Kim, H., Hsieh, I.-T., Liu, S.-Y., & Taam, R. E. 2013, *ApJ*, 776, 86  
 Kloppenborg, B., Stenel, R., Monnier, J. D., et al. 2010, *Nature*, 464, 870  
 Leinert, Ch., Graser, U., Przygodda, F., et al. 2003, *Ap&SS*, 286, 73  
 Lohmann, A. W., Weigelt, G., & Wirmitzer, B. 1983, *Applied Optics*, 22, 4028  
 Lykou, F., Klotz, D., Paladini, C., et al. 2015, *A&A*, 576, A46 (L15)  
 Maercker, M., Mohamed, S., Vlemmings, W. H. T., et al. 2012, *Nature*, 490, 232  
 Magalhães, A. M., Coyne, G. V., Codina-Landaberry, S. J., & Gneiding, C. 1986, *A&A*, 154, 1  
 Mathar, R. J. 2006, "MIDI Optical Path Differences and Phases", <http://www2.mpia-hd.mpg.de/~mathar/public/matharMIDI20051110.pdf>  
 Mauron, N., & Huggins, P. J. 2006, *A&A*, 452, 257  
 Mayer, A., Jorissen, A., Paladini, C., et al. 2014, *A&A*, 570, A113  
 Monnier, J. D., Tuthill, P. G., & Danchi, W. C. 2000, *ApJ*, 545, 957  
 Ohnaka, K., Hofmann, K.-H., Benisty, M., et al. 2009, *A&A*, 503, 183  
 Ohnaka, K., Weigelt, G., Millour, F., et al. 2011, *A&A*, 529, A163  
 Ohnaka, K., Hofmann, K.-H., Schertl, D., et al. 2013, *A&A*, 555, A24  
 Ohnaka, K. 2014, *A&A*, 568, A17  
 Petrov, R. G., Malbet, F., Weigelt, G., et al. 2007, *A&A*, 464, 1  
 Ramstedt, S., Mohamed, S., Vlemmings, W. H. T., et al. 2014, *A&A*, 570, L14  
 Richichi, A., Percheron, I., & Kristoforova, M. 2005, *A&A*, 431, 773  
 Sahai, R., & Trauger, J. T. 1998, *AJ*, 116, 1357.  
 Tatulli, E., Millour, F., Chelli, A., et al. 2007, *A&A*, 464, 29  
 Thiébaud, E. 2008, *SPIE Procs*, 7013, 70131I  
 van Leeuwen, F. 2007, *A&A*, 474, 653  
 Weigelt, G. 1977, *Optics Communications*, 21, 55  
 Weigelt, G., Balega, Y., Blöcker, T., Fleischer, A. J., Osterbart, R., & Winters, J. M. 1998, *A&A*, 333, L51  
 Whitelock, P., Marang, F., & Feast, M. 2000, *MNRAS*, 319, 728  
 Winters, J. M., Le Bertre, T., Nyman, L.-Å., Omont, A., & Jeong, K. S. 2002, *A&A*, 388, 609  
 Zhao, M., Gies, D., Monnier, J. D., et al. 2008, *ApJ*, 684, L95

## Appendix A: Removal of detector artifacts from MIDI acquisition images

As Fig. A.1a shows, noticeable vertical stripes are present in the sky-subtracted frames of the MIDI acquisition data of L<sub>2</sub> Pup. These detector artifacts presumably result from the high brightness of L<sub>2</sub> Pup (the central region within  $0''.1$  is saturated). No vertical stripes appear in the images of the PSF reference stars. The intensity of the vertical stripes is different in the upper and lower regions with respect to the star, and it therefore is necessary to remove the stripes in the upper and lower regions separately. In each region, we removed the stripes as follows. First, for each column affected by the vertical stripes, we computed the median of the pixel values from the rows sufficiently far away from the star. Then we subtracted this median from all pixels in the column. We carried out this procedure for all columns that were affected by the stripes. Figure A.1 demonstrates that the image is nearly free from the stripes after this procedure.

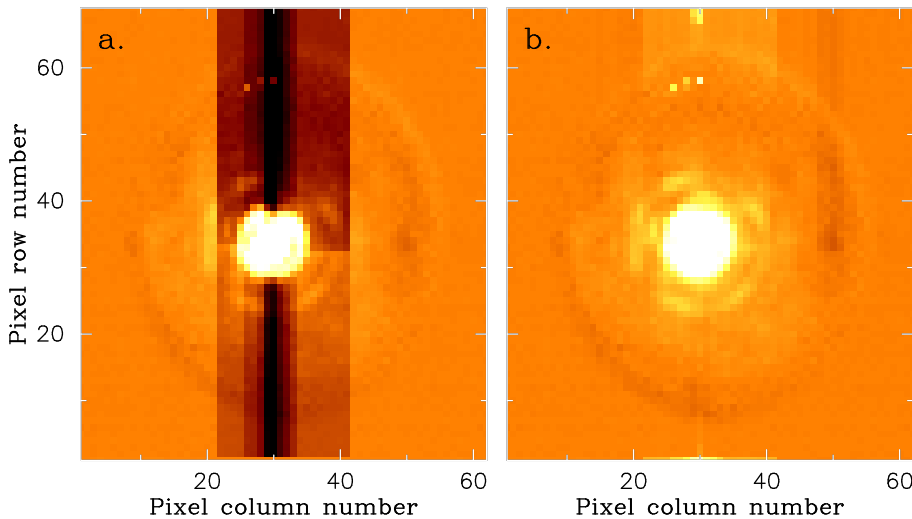


**Fig. A.1.** Removal of the detector artifacts in the MIDI acquisition images of L<sub>2</sub> Pup. **a:** One of the sky-subtracted frame of L<sub>2</sub> Pup, showing vertical stripes in the columns near the center. **b:** Same frame after the removal of the vertical stripes. The color scale in the diffraction core is saturated to clearly show the stripes.

## Appendix B: Image reconstruction

The observed visibilities plotted in Fig. 3a show a steep drop at low spatial frequencies  $\lesssim 3 \times 10^6 \text{ rad}^{-1}$  (= baselines shorter than 6 m), which suggests a very extended component. The visibilities observed at spatial frequencies from  $\sim 6 \times 10^6 \text{ rad}^{-1}$  to  $10^7 \text{ rad}^{-1}$  (baselines from 13 to 22 m) may appear reminiscent of the first and the second visibility lobe expected from a uniform disk or limb-darkened disk. However, the visibility from a uniform disk without an extended component is 0.13 (or lower for a limb-darkened disk) in the extrema of the second visibility lobe, much lower than the observed values of  $\sim 0.3$ . With an extended component as revealed by the speckle data, the visibility would be even lower. We first attempted to explain these observed data using geometrical models. While simple geometrical models may not fit the data completely, they are useful for characterizing the approximate geometry of the object and can also be used as an initial model for the image reconstruction.

### Appendix B.1: Geometrical model: uniform disk + elliptical Gaussian

We tried to fit the data with a geometrical model consisting of a uniform-disk-like central star and an elliptical Gaussian. The free parameters are the uniform-disk diameter of the central star ( $\phi_\star$ ), the fractional flux contribution of the central star  $f_\star$ , the widths of the elliptical Gaussian along the major and minor axes  $\sigma_{\text{major}}$  and  $\sigma_{\text{minor}}$  (the elliptical Gaussian is given by  $e^{-((x/\sigma_{\text{major}})^2 + (y/\sigma_{\text{minor}})^2)}$ ), and the position angle of its major axis PA (measured from North to East). We searched for the best-fit model by varying  $\phi_\star = 8 \dots 22$  (mas) with  $\Delta\phi_\star = 2$  (mas),  $f_\star = 0.1 \dots 0.7$  with  $\Delta f_\star = 0.05$ ,  $\sigma_{\text{major}} = 30 \dots 100$  (mas) with  $\Delta\sigma_{\text{major}} = 10$  (mas),  $\sigma_{\text{minor}} = 10 \dots 50$  (mas) with  $\Delta\sigma_{\text{minor}} = 10$  (mas), and PA =  $70^\circ \dots 100^\circ$  with  $\Delta\text{PA} = 5^\circ$  (the PA was limited to this range from the elongation of the image reconstructed from the speckle data alone). The best-fit model, which is plotted in Fig. B.1, is characterized by  $\phi_\star = 12$  mas,  $f_\star = 0.3$ ,  $\sigma_{\text{major}} = 50$  mas,  $\sigma_{\text{minor}} = 20$  mas, and PA =  $95^\circ$  with a reduced  $\chi^2$  of 27.2. Figure B.1 reveals that the best-fit model cannot reproduce the observed visibilities at spatial frequencies of  $(0.6 - 2.0) \times 10^7 \text{ rad}^{-1}$  (baseline length = 13–44 m). Most of the observed visibilities at these spatial frequencies are noticeably higher than predicted by the model. This means that there is some sharp structure that is not seen in the smooth Gaussian model.

### Appendix B.2: Geometrical model: uniform disk + elliptical ring

We then tried a model consisting of the uniform-disk-like central star and an elliptical ring, because a ring gives rise to visibilities much higher than a uniform disk or limb-darkened disk at long baselines. The free parameters are the uniform-disk diameter of the central star  $\phi_\star$ , the fractional flux contribution of the central star  $f_\star$ , the semi-major and semi-minor axes of the elliptical ring ( $R_{\text{major}}$  and  $R_{\text{minor}}$ , respectively), and its position angle PA. The width of the ring was set to be 10% of its radius at each position angle. We searched for the best-fit model by varying  $\phi_\star = 8 \dots 22$  (mas) with  $\Delta\phi_\star = 2$  (mas),  $f_\star = 0.1 \dots 0.6$  with  $\Delta f_\star = 0.05$ ,  $R_{\text{major}} = 30 \dots 100$  (mas) with  $\Delta R_{\text{major}} = 10$  (mas),  $R_{\text{minor}} = 10 \dots 50$  (mas) with  $\Delta R_{\text{minor}} = 10$  (mas), and PA =  $70^\circ \dots 100^\circ$  with  $\Delta\text{PA} = 5^\circ$ . Figure B.2 shows a comparison of the best-fit ring model with the observed data. This model is characterized by  $\phi_\star = 16$  mas,  $f_\star = 0.6$ ,  $R_{\text{major}} = 60$  mas,  $R_{\text{minor}} = 40$  mas, and PA =  $95^\circ$  with the reduced  $\chi^2 = 54.8$ . While the visibilities at  $(0.6 - 1) \times 10^7 \text{ rad}^{-1}$  from this model is as high as or even higher than the observed data, the fit to the speckle data and the data at longer baselines is worse than the above star + Gaussian model as shown by the worse reduced  $\chi^2$ .

### Appendix B.3: Geometrical model: obscured uniform disk + elliptical Gaussian

We found out that the observed data are much better reproduced if the southern half of the aforementioned uniform-disk-like central star + elliptical Gaussian model is obscured. In this model, the intensity of the uniform-disk star + elliptical Gaussian model  $I_0(x, y)$  ( $x$  and  $y$  are the coordinates on the sky with the origin at the central star) is modified as follows:

$$I(x, y) = I_0(x, y) \times \frac{1}{e^{-y/\varepsilon} + 1},$$

where  $\varepsilon$  is a parameter to smoothen the obscuration edge. We set  $\varepsilon$  to be 0.2, which decreases the intensity to zero over  $\sim 2$  mas in the  $y$  direction. The free parameters are the uniform-disk diameter of the central star, the fractional flux contribution of the central star  $f_\star$ , the widths of the elliptical Gaussian along the major and minor axes  $\sigma_{\text{major}}$  and  $\sigma_{\text{minor}}$ , and the position angle of its major axis PA. We searched for the best-fit model by varying  $\phi_\star = 8 \dots 22$  (mas) with  $\Delta\phi_\star = 2$  (mas),  $f_\star = 0.2 \dots 0.6$  with  $\Delta f_\star = 0.05$ ,  $\sigma_{\text{major}} = 30 \dots 100$  (mas) with  $\Delta\sigma_{\text{major}} = 10$  (mas),

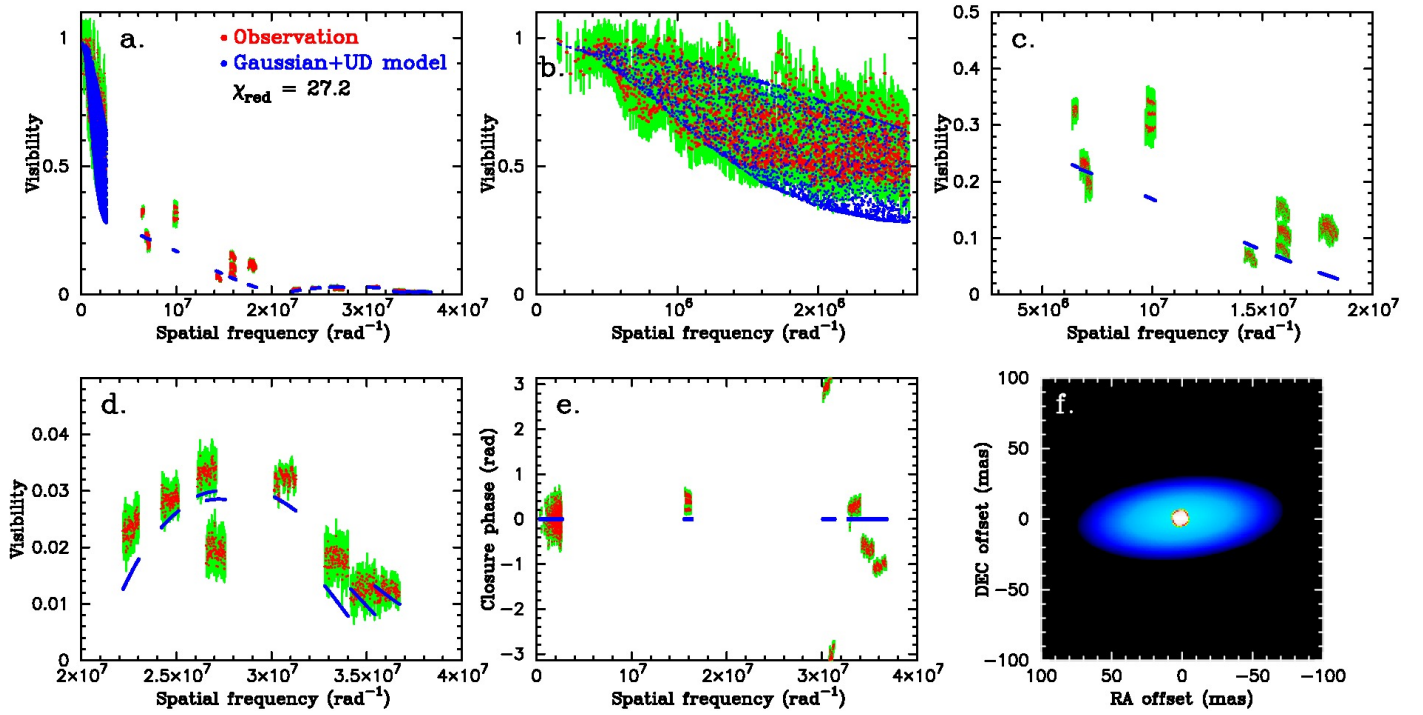


Fig. B.1. Best-fit model consisting of a uniform-disk central star and an elliptical Gaussian shown in the same manner as Fig. 6.

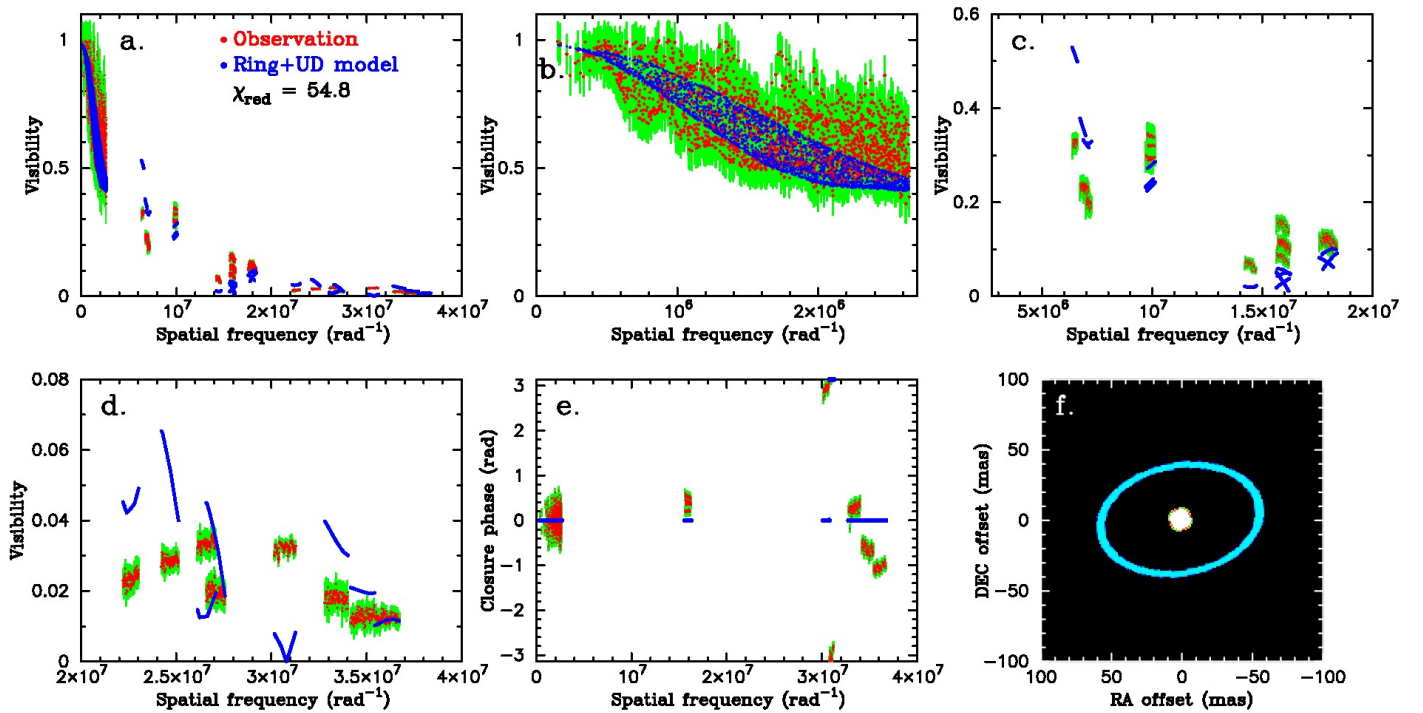
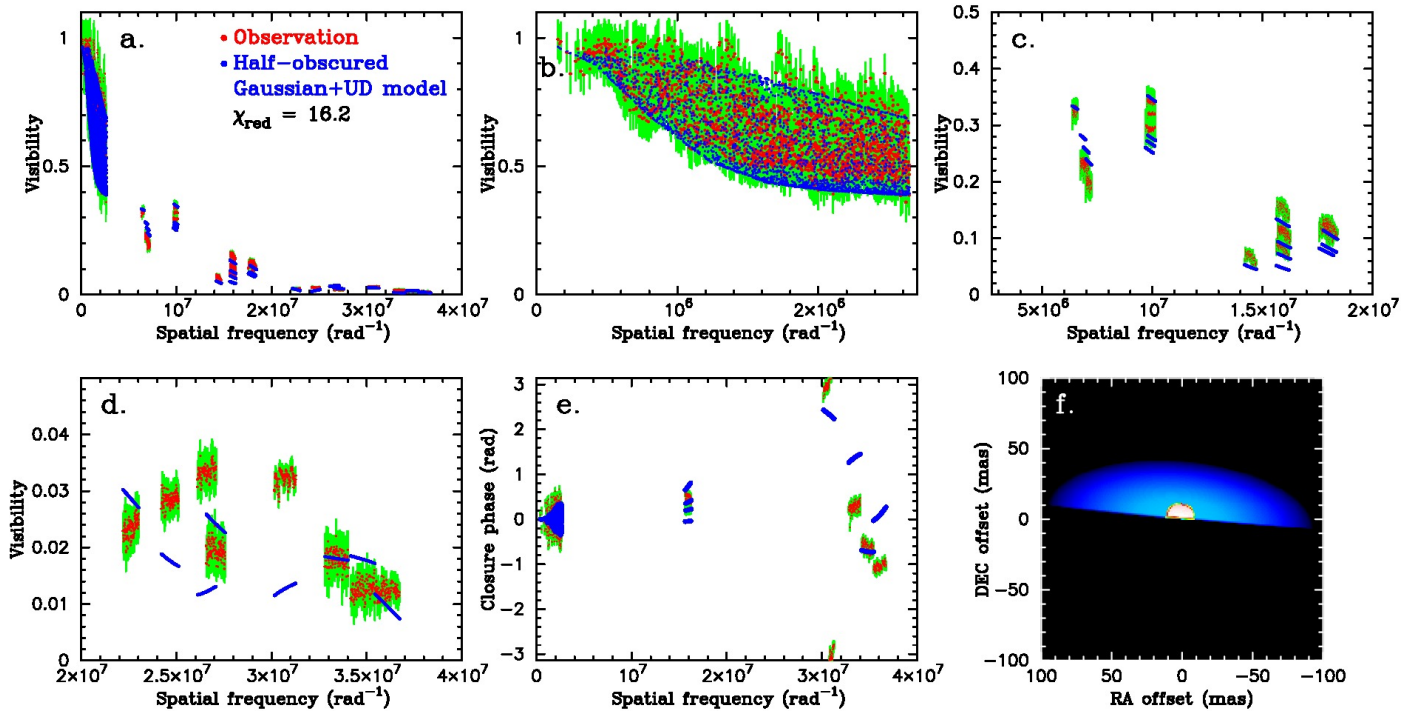


Fig. B.2. Best-fit model consisting of a uniform-disk central star and an elliptical ring shown in the same manner as Fig. 6.

$\sigma_{\text{minor}} = 10 \dots 50$  (mas) with  $\Delta\sigma_{\text{minor}} = 10$  (mas), and  $\text{PA} = 70^\circ \dots 100^\circ$  with  $\Delta\text{PA} = 5^\circ$ .

The best-fit model is characterized by  $\phi_\star = 20$  mas,  $f_\star = 0.45$ ,  $\sigma_{\text{major}} = 70$  mas,  $\sigma_{\text{minor}} = 30$  mas, and  $\text{PA} = 85^\circ$ . As Fig. B.3 shows, this model can reproduce the observed visibilities much better than the above two models. The uncertainties in  $f_\star$ ,  $\sigma_{\text{major}}$ ,  $\sigma_{\text{minor}}$ , and  $\text{PA}$  are  $\pm 0.05$ ,  $\pm 10$  mas,  $\pm 10$  mas, and  $\pm 5^\circ$ . The uniform-disk diameter of the central star is in the range between 18 and 20 mas. This agrees with the 17.5 mas derived by K14, given the difference in the data and the model used by

them and us. The reduced  $\chi^2$  of this model is 16.2, which is much better than the star + Gaussian or star + ring models, but still much larger than 1. This is because the fit to the visibilities observed at the longest baselines (spatial frequencies higher than  $\sim 2 \times 10^7 \text{ rad}^{-1}$ ) and to the observed closure phases are not satisfactory. However, this disagreement can be due to small-scale structures that are not included in our geometrical model, but can be modeled by the image reconstruction.



**Fig. B.3.** Best-fit model consisting of a half-obscured uniform-disk central star and an elliptical Gaussian shown in the same manner as Fig. 6.

#### Appendix B.4: MiRA parameters

We used the best-fit half-obscured star + elliptical Gaussian model as the initial model. The regularization scheme of the maximum entropy method was adopted, with the prior being the Gaussian with the same widths as the initial model. The degree of regularization was set to  $\mu = 10^3$  (see Thiébaud 2008 for details of the regularization scheme and the definition of  $\mu$ ). We also reconstructed the image with the total variation regularization scheme, but the image shows no noticeable differences.